liquids

MDPI

Article

Liquid Springs from Wettable Materials

Dusan Bratko * and Ao Sterner

Department of Chemistry, Virginia Commonwealth University, Richmond, VA 23284-2006, USA
* Correspondence: dbratko@vcu.edu

Abstract

Conventional liquid springs enable storage of energy in the form of interfacial tension at forcibly wetted lyophobic surfaces. The pressure–volume work performed to compress the liquid into a poorly wettable porous medium is recovered during spontaneous expulsion when pressure falls below the capillary pressure characteristic of a given system. Our study explores generalizations to easily wettable materials where liquid infiltration is opposed solely by steric hindrance exerted on liquid molecules in micro-sized pores. The concept is exemplified in molecular simulations of prototypical model systems with methanol intruding narrow slits between hydrocarbon or graphene surfaces. While these materials show significant wetting propensities at macroscopic interfaces with liquid methanol, substantial compression is required to wet molecular-sized pores barely accommodating a monolayer of liquid molecules. The observed O(10^3) bar intrusion pressures secure stored energy densities competitive with supercapacitors and amenable to improvement. Wall–liquid attraction and small pore diameters lead to intrusion–expulsion pathways along cooperative-adsorption isotherms. The process avoids abrupt liquid/vapor transitions and associated nucleation barriers, responsible for cycle hysteresis in experiments with water in hydrophobic capillaries. Using open ensemble (Grand Canonical) Monte Carlo sampling, we identify the range of porosities supporting reversible energy storage/recovery operation in lyophilic media; the results can assist with the design of molecular spring devices with competitive storage and power capacities in pragmatic contexts.

Keywords: wetting propensity; micropore adsorption; reversible cycling; molecular simulation

1. Introduction

The free energy increase associated with the formation of an interface between a liquid and a poorly wettable solid underlies the function of energy absorption devices like liquid springs [1], shock absorbers, or bumpers, classified [2–6] according to their ability for complete, partial, or negligible energy recovery. According to continuum theory of capillarity [7], the stored energy can be estimated as the product $A\Delta\gamma$ where A is the liquid/solid contact area and $\Delta\gamma = \gamma_{sl} - \gamma_{sv}$ the wetting free energy:

$$\Delta\gamma = -\gamma cos\theta \ \sim \ a\, P_{in} h \tag{1}$$

where γ is the liquid's surface tension and γ_{sl} and γ_{sv} the solid–liquid and solid–gas interfacial free energies, P_{in} is the open ensemble intrusion pressure from the Kelvin equation for pore diameter h, a is a geometry-dependent factor (1/2, 1/4, or 1/6 for planar, cylindrical, and spherical pores, respectively), and θ is the contact angle on a macroscopic surface of given solid [8,9]. Ideally, liquid intrusion and energy absorption take place at external pressures above P_{in} determined in Equation (1) and the energy can be recovered in the form

Academic Editor: Enrico Bodo

Received: 31 March 2026
Revised: 17 May 2026
Accepted: 29 May 2026
Published: 3 June 2026

of pressure–volume work during spontaneous expulsion when pressure is reduced below the intrusion threshold. The above relations limit materials' choices to lyophobic substances characterized by solid/liquid contact angles above 90 degrees. Continuum approximation, however, becomes less reliable in microporous materials with extreme specific surface area, e.g., zeolites or metalorganic frameworks (MOF-s), which are favored in energy absorption devices because of their high storage capacity [10,11]. At pore diameters comparable to molecular size, steric restrictions interfere with liquid uptake (See Section 2), resulting in positive intrusion pressures and wetting free energies irrespective of the nominal lyophilicity of free-standing material [12]. Using molecular models of methanol in moderately and strongly lyophilic micropores, we show how tuning of pore dimensions can lead to viable liquid spring operation with an additional advantage of overcoming the cycling hysteresis commonly observed with hydrophobic solid/water combinations. Since the liquid content in the pores varies with external conditions, molecular simulations require open ensemble (μ, V, T) sampling, performed here by Grand Canonical Monte Carlo (GCMC) method [13–15]. Above, μ is the pressure-dependent liquid's chemical potential, and V and T denote volume and temperature. Calculation of the chemical potential as a function of pressure in the bulk phase (P_b) therefore represents the first stage of the study. Once completed, the bulk-phase results are used to determine the changes in liquid content and structure in the pores equilibrated with pressurized bulk. By systematically varying the bulk pressure, we identify a window of pressures replacing a unique 'intrusion pressure' (P_{in}) at different pore sizes. The comparison between systems with methanol adsorbed to softer (hydrocarbon) or stiffer (graphene [16]) pore walls reveals a significant difference between the two materials, with a comparatively wider range of pore widths supporting liquid spring behavior in the former case and a very narrow range in the latter one. In both materials, reversible filling–emptying cycling is restricted to monolayer pore widths, and the process proceeds along adsorption isotherms distinct from the first-order liquid–vapor transitions typically observed in strongly lyophobic systems.

2. Models and Methods

The model adsorbent is represented by a collection of planar pores between parallel hydrocarbon or graphene surfaces separated by a subnanometer distance h. The pores are attributed mesoscopic dimensions implemented through lateral (x, y) periodicity with a replicating-box size $L_x = L_y$ between 25 and 50 Å. For the sake of simplicity, in this idealized adsorbent geometry [17], we refrain from including any wall functionalities necessary to fix the wall-to-wall separation in adsorbent synthesis. The values of h vary between the thicknesses of one to two monolayers of absorbed methanol. Because of the perceived independence of individual pores, a single pore is treated as a representative repeating unit of a macroscopic porous medium. Figure 1 illustrates a simulation box of a graphene/methanol system.

Interatomic potentials involving methanol were described according to the TraPPE force field [18], and we used parameterizations for graphene and hydrocarbon from previous works in this group [19–21]. Nonelectrostatic interatomic potentials are described in terms of Lennard-Jones interactions with energy and size parameters ε and σ of 773 J mol^{-1} and 3.02 Å for oxygen atoms, 814.8 J mol^{-1} and 3.75 Å for CH_3 groups in methanol, 236 J mol^{-1} and 3.214 Å for graphene carbons, and 648 J mol^{-1} and 3.742 Å for hydrogenated carbon atoms in hydrocarbon. Being buried deep inside the van der Waals radii of carbon or oxygen atoms, hydrogens do not make independent contributions to Lenard-Jones interactions [18]. Lorentz–Berthelot mixing rules [14] were applied to describe interactions among unequal atoms. Interactions with graphene walls were calculated by explicit atom–atom summations, whereas we used integrated (9-3 Lennard-Jones) wall/liquid

interactions based on spatially averaged atom density for hydrocarbon walls [12,22–24]. In contrast to the original derivation [22], spatial integration was performed with underlying 12-6 Lennard-Jones potentials truncated at the cutoff distance of 12 Å, which leads to the convergence with respect to wall thickness $\delta_w \geq$ ~9 Å. In narrow pores, the interaction between liquid molecules and the adsorbent represents the superposition of potentials from both confining walls. Figure 2 shows laterally averaged methanol/adsorbent interaction profiles for several pore widths h between 5 and 10 Å for the parallel molecular orientation (methanol O and C atoms at the same distance from the pore midplane), which is prevalent at tight pore dimensions.

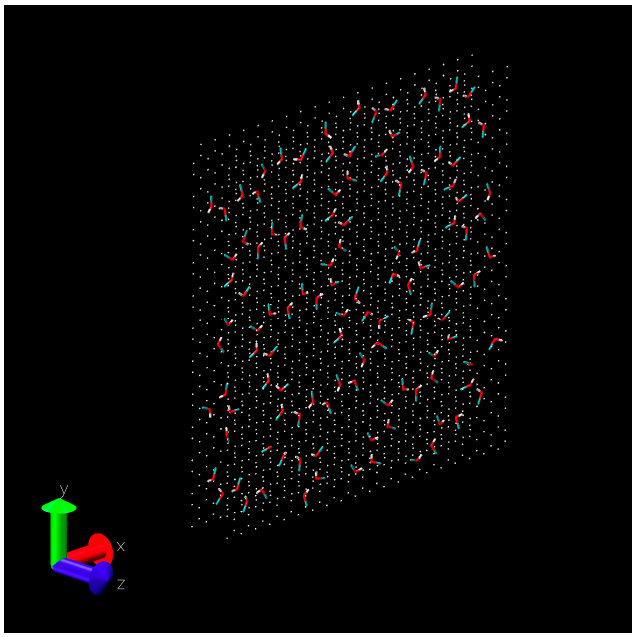

Figure 1. A VMD-generated snapshot of a replicating Monte Carlo cell with a monolayer of methanol between parallel ~50 Å × 50 Å graphene layers (light grey) at separation h = 7 Å. Note the omission of C-C bonds and reduced atom sizes used to improve the visibility of confined liquid (red: O, white: H, and green: CH_3).

In addition, methanol molecules featured Coulombic interactions corresponding to partial charges −0.7, 0.435 and 0.265 e_o on O, H, and CH_3, respectively [18]. In view of lateral periodicity, electrostatic interactions were augmented by slab-corrected Ewald summation [25] whereas we use conventional 3-dimensional Ewald sums [26] in bulk phase calculations. A smooth cutoff at a distance of 12 Å with no tail correction was applied to both the interatomic Lennard-Jones potentials and the real term representing shielded Coulombic interaction in Ewald summation.

In the first approximation, our models neglect internal degrees of freedom of methanol molecules and adsorbent walls. As such, they cannot capture molecular polarizability effects and any structural changes in the adsorbent at high compression. A favorable comparison between the computed and measured densities indicates acceptable performance of the Trappe model over a broad pressure range. While our methods allow generalizations to nonrigid adsorbent models, in view of computational restrictions, we defer assessing sensitivity to respective refinements for future studies with detailed full-atom representations of specific adsorbents.

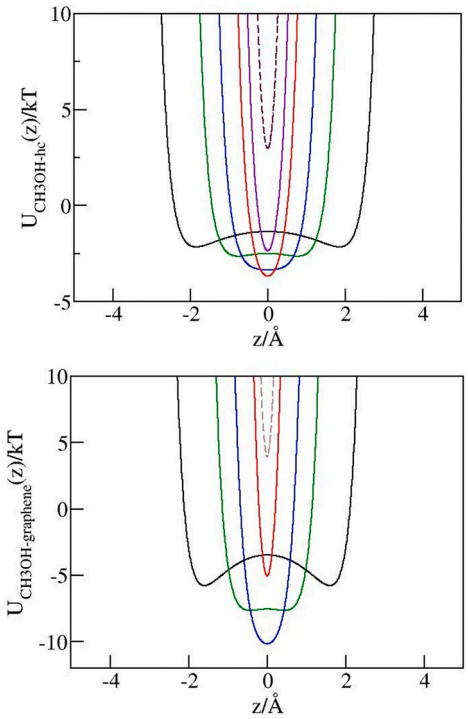

Figure 2. Averaged liquid/adsorbent potential profiles across planar hydrocarbon (top) and graphene micropores (bottom) as a function of perpendicular coordinate z for parallel walls positioned at ±h/2 (h is measured between the centers of exposed wall atoms); h = 10 (black), 8 (green), 7 (blue), 6 (red), and 5.5 Å (violet), all for parallel molecule/wall orientation. Purely repulsive 5 Å hydrocarbon pores (dashed maroon) and 5.7 Å graphene pores (dashed light brown) are included to illustrate the trends but were not considered in the simulations.

Operation of liquid springs involves pressure-dependent absorption of liquid molecules from compressed surroundings, and their release upon decompression. The changing liquid content inside the pores was determined using Grand Canonical Monte Carlo (GCMC) simulations [13,14] implemented in analogy with previous works [12,17,19,24,27]. The in-house GCMC code has been adapted from ref. [19] with subsequent incorporations of 2-dimensional Ewald summation [25] and routines relating chemical potential to density and pressure in a liquid reservoir [12]. According to the formulation of Adams [28,29], the number of liquid molecules inside a specified volume V approaches the equilibrium value for given bulk pressure P_b when randomly attempted additions ($N \rightarrow N+1$) and deletions ($N \rightarrow N-1$) are accepted with probabilities

$$acc_{N\rightarrow N+1} = min\left\{1,\ \frac{<N>}{N+1} e^{\beta[\mu_{ex}(P_b)-\Delta U]}\right\} \quad (2)$$

$$acc_{N\rightarrow N-1} = min\left\{1,\ \frac{N}{<N>} e^{\beta[-\mu_{ex}(P_b)-\Delta U]}\right\}$$

Above, N denotes the current number of molecules in a given volume, <N> the average N in an identical volume in bulk liquid, $\beta = 1/kT$ where kT is the thermal energy, $\mu_{ex}(P_b)$ the pressure-dependent excess chemical potential and ΔU the energy change associated with the attempted addition or deletion. Compared to modeling of molecular exchanges between the pore and *explicit* reservoir of bulk liquid, doable in Molecular Dynamics simulations, the GCMC method presents an efficiency advantage by omitting the reservoir (many times bigger than the pore), although the process is impeded by low exchange acceptances, typically of O(10^{-4}) in confinement and about twice as low in the bulk. Exchange move attempts are accompanied by random translations and rotations accepted

according to the conventional Metropolis algorithm [13,14]. A typical number of attempted Monte Carlo moves of order of 10^9 is required for combined equilibration and production calculation of liquid content, with run length gradually increasing with pressure because of lowered exchange acceptances at tightened molecular packing in the liquid. Property averages over n_b = O(10^3) blocks, with O(10^4) passes [30] per block, were analyzed based on the evidence of insignificant correlations [30] between consecutive blocks of specified size. Error bars for the total averages, σ_t, were hence estimated [31] as $\sigma_t \approx \sigma_b/\sqrt{n_b}$, where σ_b denotes standard deviation of the averaged property for individual blocks.

Application of Equation (2) in the pores requires the knowledge of excess chemical potential of methanol as a function of pressure in the bulk phase. In principle, this can be achieved by determining bulk pressures in a series of GCMC simulations for preselected values of chemical potentials. This straightforward approach, however, proves increasingly time-consuming at pressures above around 2000 bar. To determine chemical potentials over a broader pressure interval, we replaced GCMC (μ, V, T) calculations in bulk liquid by canonical (N, V, T) Monte Carlo simulations of pressures in a set of runs performed at preselected number densities of the liquid and used the pressure/density relation to determine the increase in chemical potential with P_b by numerical integration using relations:

$$\mu(P_b) = \mu(P_o) + \int_{P_o}^{P_b} \overline{V}(P)\, dP = \mu(P_o) + \int_{P_o}^{P_b} \frac{1}{\rho(P)}\, dP \tag{3}$$

and

$$\mu_{ex}(P_b) = \mu_{ex}(P_o) + \int_{P_o}^{P_b} \frac{1}{\rho(P)}\, dP - kTln\frac{\rho(P_b)}{\rho(P_o)} \tag{4}$$

Above, $\overline{V}(P) = \frac{1}{\rho(P)}$ is the partial molar volume and $\rho(P) = \frac{<N>}{V}$ the number density of the liquid at given pressure, P_o is bulk pressure at ambient conditions (1 bar and 298 K), and we determine the excess chemical potential $\mu_{ex}(P_o) = -8.194 \pm 0.002\, kT$ as the value leading to the desired standard state pressure P_o = 1 ± 10 bar. Bulk pressure P_b, or parallel and perpendicular pressure components, $P_\parallel$ and $P_\perp$ in confined systems, were calculated according to the finite difference approximation [19,32]

$$P_\delta = \frac{<N>}{V}kT - \frac{1}{kt}\lim_{\Delta V_\delta \to 0} < \frac{\Delta U_\delta}{\Delta V_\delta} >, \tag{5}$$

detailed in previous work [19]. Above, ΔU_δ is the energy difference associated with tiny trial volume change ΔV_δ and subscript δ (b, $\parallel$, or$\perp$) signifies isotropic volume scaling (b), vs. scaling along lateral ($\parallel$), or perpendicular ($\perp$) directions. For planar pores open to liquid exchange with bulk surroundings, $-P_\parallel$ equals intrusion pressure P_{in}, Equation (1). In wider pores where the opposing interfaces are essentially independent of each other, open ensemble calculations of $P_\parallel$ therefore yield macroscopic wettability estimates for the model hydrocarbon- and graphene–methanol systems considered in our study.

Chemical potentials $\mu_{ex}(P_b)$ were used in GCMC simulations of micropores of different diameters in equilibrium with (implicit) bulk reservoir of liquid methanol. In a series of runs, the reservoir pressure P_b was gradually increased, and we monitored the rising content of the liquid as a function of compression. When the pores were completely filled, the process was reversed to check for the possible hysteresis of the cycle, and the process continued until complete expulsion or reaching the ambient pressure in the bulk phase.

3. Results and Discussion

3.1. Liquid Methanol at Elevated Pressures

Figure 3 (top) illustrates the dependence of number density $\rho_b = <N>/V$ of liquid methanol on pressure P_b determined using canonical (N,V,T) Monte Carlo simulations for

a set of densities preselected according to accessible experimental data [33,34]. Despite the simplifications of the model potential for methanol [18], the computed function $\rho_b(P_b)$ agrees well with the experiment, both giving a 35% density increase upon compression over the measured interval from 1 to 8000 bar. The solid line in Figure 3 (top) represents an empirical fitting function $\rho_b(P_b) = [14.32 + 4.937 \times 10^{-3}(P_b/P_o) - 1.182 \times 10^{-3}(P_b/P_o)^{1.2} + 0.774 \times 10^{-4}(P_b/P_o)^{1.4}]$ nm^{-3} used in calculations of chemical potential (solid curve in Figure 3 bottom) according to Equation (4). P_o = 1 bar. To test the reliability of the procedure, excess chemical potentials for pressures of up to 2.5 kbar were also reproduced in explicit GCMC calculations. These results, presented as open circles in Figure 3 (bottom), show excellent agreement with predictions from Equation (4). In view of decreasing GCMC exchange acceptances, at higher pressures the accuracy of the indirect route (Equation (4)) becomes superior to GCMC calculations.

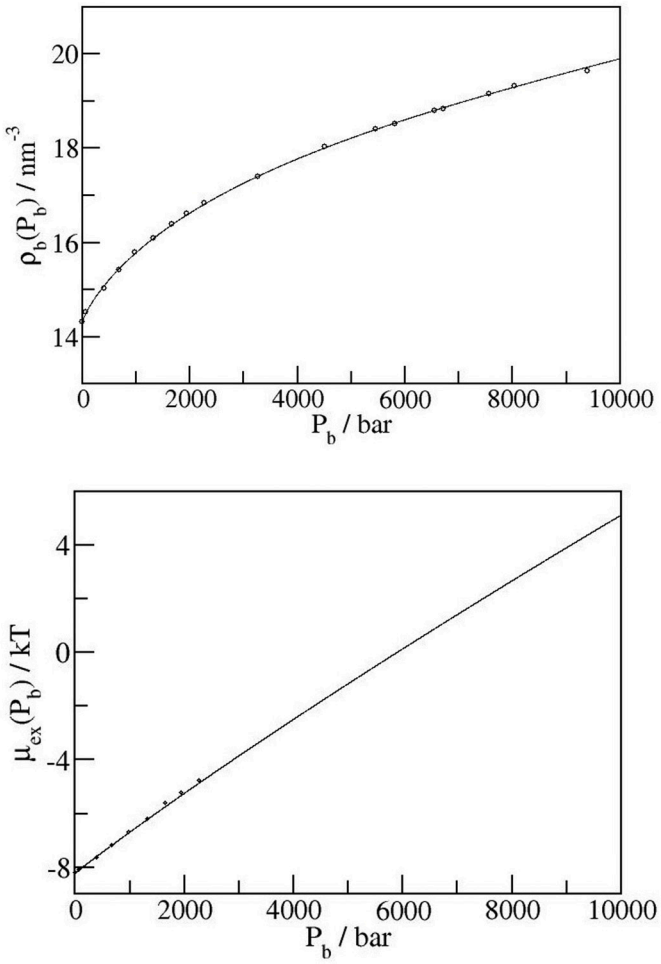

Figure 3. (Top): Simulated (circles) and fitted (solid curve) number densities of bulk methanol as a function of pressure from canonical (N, V, T) Monte Carlo simulations. (Bottom): Excess chemical potential of methanol as a function of pressure determined using simulated number densities and numerical integration of Equation (4) (solid curve), compared to the results of explicit GCMC (μ, V, T) simulations (open circles) at moderate pressures P_b.

3.2. Characterization of Macroscopic Wettabilities of Model Hydrocarbon and Graphene Surfaces

Capillarity theory provides reasonable predictions of pore thermodynamics at pore diameters $h \geq 2$ nm [9,35,36]. Relying on Equation (1) and the equality $P_{in} = -P_{\|}$, we exploit GCMC calculations to estimate methanol contact angles above hydrocarbon and graphene surfaces from simulated $P_{\|}$ in 3 nm pores with walls from the above materials, in equilibrium with a methanol bath at ambient conditions. Both systems manifest lyophilic

behaviors ($\Delta\gamma < 0$). In hydrocarbon pore, $\Delta\gamma \sim -9.5 \pm 1$ mN m^{-1} and relation $\theta = cos^{-1}\left(-\frac{\Delta\gamma}{\gamma}\right) = cos^{-1}\left(\frac{hP_{||}}{2\gamma}\right)$ yields $\theta \sim 65 \pm 3°$. In the case of graphene, $-\Delta\gamma > \gamma$ suggesting complete wetting ($\theta \to 0$) as could have been expected in view of stronger wall/liquid attraction shown in Figure 2. The above behaviors are affirmed by snapshots of methanol clusters (270 molecules per 25 nm^2) on single surfaces of either solid shown in Figure 4, with moderately lyophilic droplets (contact angle well under 90°) on hydrocarbon, and uniform spreading over the entire available area, characteristic of vanishing contact angle on graphene sheet.

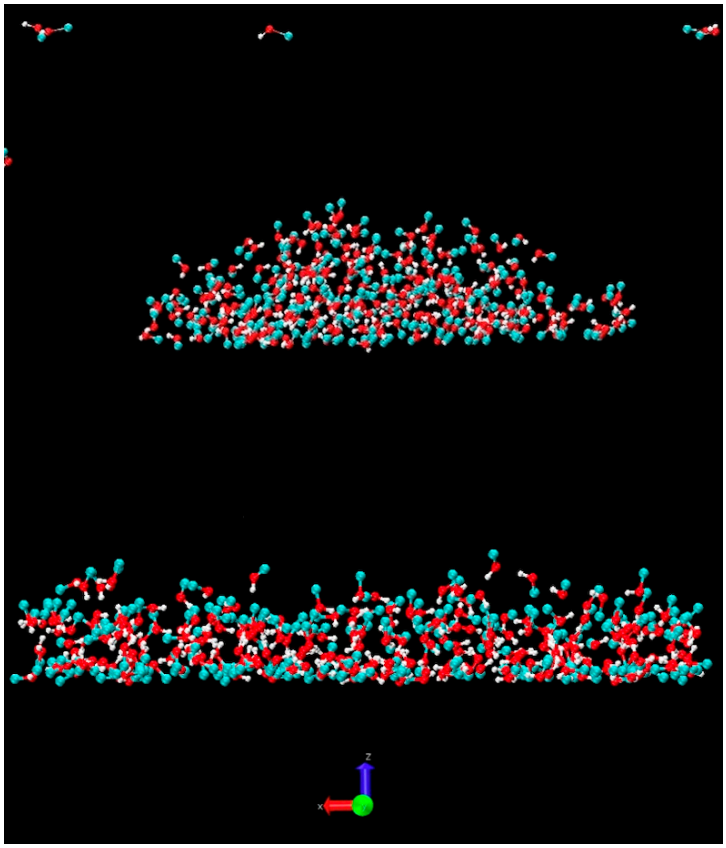

Figure 4. Snapshots showing representative structures of 270 methanol molecules atop a 50 Å × 50 Å hydrocarbon surface (top) or graphene sheet (bottom). Periodic boundary conditions applied along lateral directions result in a semi-infinite liquid layer on graphene as opposed to individual replica drops on hydrocarbon.

3.3. Pressure-Controlled Methanol Absorption and Desorption in Micropores

In view of their wetting propensities, wider pores between hydrocarbon or graphene surfaces in contact with liquid methanol spontaneously fill with the liquid at ambient pressure in the bulk phase. The trend is, however, reversed in narrower pores (diameter h below 1 nm), where steric restrictions suppress both translational and rotational entropies and, for pore widths below about twice the wall/liquid atom contact distance, gradually increase the wall/methanol interaction potential (Figure 2). In a series of GCMC simulations at ambient bulk pressure, spontaneous expulsion from an initially filled hydrocarbon pore was observed for pore widths $h \leq 9.7 \pm 0.1$ Å. Upon further narrowing of the pores, expulsion becomes feasible at elevated pressures of interest to increase the amount of energy that can be stored in the pores. Pore widths exceeding the expulsion threshold (9.7 Å), on the other hand, preclude liquid spring operation and were no longer considered. Below, we present the results of systematic GCMC simulations of pore filling as a function of bulk pressure P_b for a set of pore diameters (measured as the distance between the liquid-

exposed carbon atoms of the opposing pore walls) h = 9.5, 8, 7, 6, and 5.5 Å. In all these cases, the pore interior includes regions of strongly attractive adsorbent/adsorbate interaction with potential energy minima $u_{min}(z)$ ranging from −2.2 to −3.7 kT in hydrocarbon pores and from −5.0 to −10.2 kT in graphene ones. The lowest values correspond to separations h of about twice the distance z minimizing $u(z)$ at a single wall. To facilitate the comparison of liquid contents obtained at different lateral box sizes, typically with L_{xy} = 25 Å or 50 Å, all the average numbers of methanol molecules <$N(P_b)$> shown in Figure 5 are prorated to a lateral area of 6.25 nm^2. To examine the possibility of cycling hysteresis, we compare dependences of <N> on P_b corresponding to intrusion or extrusion processes mimicked by calculating <N> in sequences of increasingly compressed (intrusion curve) or decompressed states (extrusion curve).

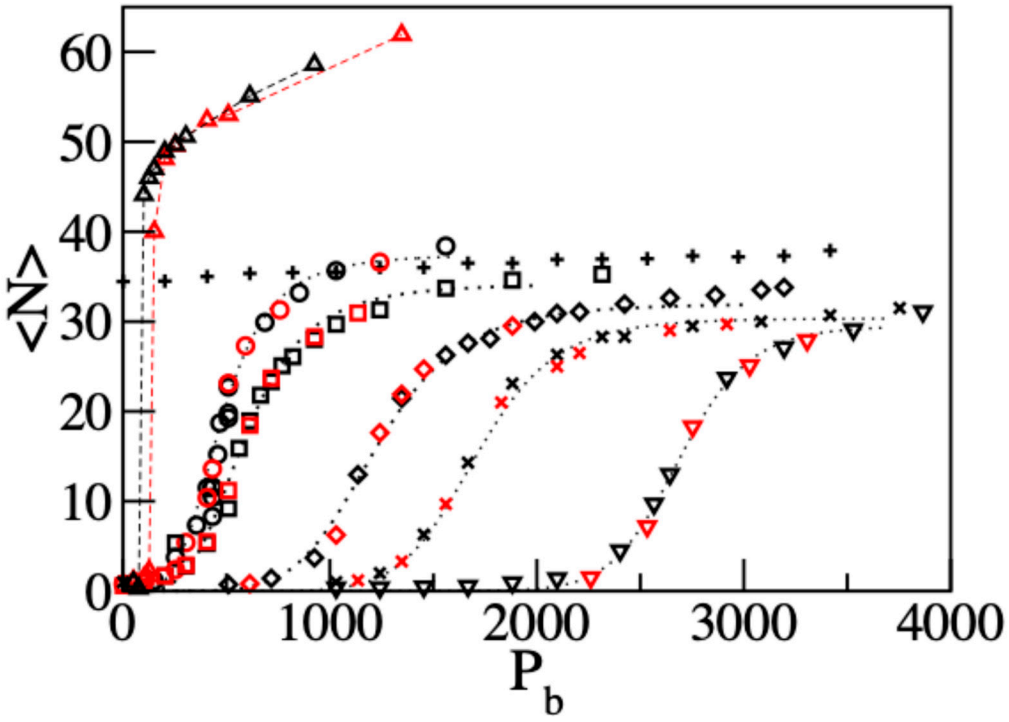

Figure 5. Methanol content in hydrocarbon (open symbols) or graphene (+, ×) micropores of width 9.5 Å (triangle up), 8 Å (circle), 7 Å (square or +), 6 Å (diamond or ×), 5.5 Å (triangle down). To facilitate comparison between the simulation results obtained at two different box sizes, L_{xy} = 25 Å or 50 Å, all values of <N> are prorated to a wall area of Å = 6.25 nm^2. Symbol sizes match estimated simulation uncertainties. Red symbols correspond to GCMC states along intrusion isotherms generated by consecutive pressure increases (beginning with ambient pressure) and the black ones to states on the extrusion curves, visited by consecutive decompression steps after initial over-compression. Dashed curves for 9.5 Å pore (triangles up) are a guide to the eye. Dotted curves represent Hill adsorption isotherms (Equation (6)) with exponents n = 4 for 8 Å (circles) and 7 Å (squares) hydrocarbon pores, n = 6 in 6 Å hydrocarbon pore (diamonds), n = 9 in 6 Å graphene pore (×) and n = 16 in 5.5 Å hydrocarbon pore (triangles down).

Except for the 9.5 Å width, which accommodates two molecular layers of absorbed methanol, a single layer of liquid molecules was observed at all the other widths. Inspection of intrusion–extrusion cycles illustrated in Figure 5 reveals a qualitative difference between the widest (9.5 Å) hydrocarbon micropore and all the other systems. While the wider system undergoes an abrupt liquid/vapor transition with considerable and reproducible hysteresis reminiscent of the behavior of lyophobic water/hydrocarbon systems [12], all the

other systems undergo gradual and completely reversible monolayer adsorption processes that follow Hill's adsorption isotherm [37,38]:

$$< N(P_b) >= a\frac{KP_b^n}{1+KP_b^n} = 2 < N(P_{in}) > \frac{\left(\frac{P_b}{P_{in}}\right)^n}{1+\left(\frac{P_b}{P_{in}}\right)^n} \quad (6)$$

where $K \cong P_{\text{in}}{}^{-\text{n}}$ and we define intrusion pressure P_{in} as the pressure at the inflection point of the adsorption isotherm (half-complete filling); $a = 2<N(P_{\text{in}})>$ approximates the saturation value of $<N>$ (ignoring finite compressibility of the confined layer beyond the adsorption transition). Values of n exceeding unity signify cooperative adsorption consistent with the formation of molecular clusters of average size roughly commensurate with n. The Hill adsorption isotherms for monolayer systems ($h \leq 8$ Å) are shown as dotted curves with fitted values of n increasing from 4 at the lowest $P_{\text{in}} \cong 590$ bar at $h = 8$ Å to $n = 16$ at the highest intrusion pressure $P_{\text{in}} \cong 2670$ bar at $h = 5.5$ Å. The complete set of applicable exponents n is given in the caption of Figure 5.

Examination of simulation snapshots (Figure 6) shows methanol molecules forming chainlike or ring clusters with most of the molecules participating in two bonds, in one as proton donor and in one as acceptor. The simulated cluster sizes showed considerable polydispersity over a typical range of 5–24 molecules per cluster. After accounting for cluster continuity across periodic box boundaries, the (arithmetic) averages of cluster sizes in all the monolayer systems followed the trend discerned from empirical values of n fitting Equation (6) (see caption of Figure 6) with somewhat higher absolute values (ranging from 7 to 19.5 as opposed to the range from 4 to 16, which provides ideal fit to the simulated adsorption isotherms). Smaller empirical values of n are likely attributable to nonlinear averaging of effective cluster sizes in polydisperse systems. Interactions among clusters appear weak, explaining gradual pore filling in contrast to the abrupt gas-to-liquid transition observed [12] in aqueous micropores. Side-by-side comparison between the snapshots of lyophilic pores partially filled with methanol and those with water between hydrophobic walls [12] reveals two distinct behaviors: aqueous and multiple-layer methanol systems ($h \geq 9.5$ Å) show coexisting vapor and liquid domains, whereas methanol monolayers at $h \leq 8$ Å behave as a two-dimensional gas of methanol clusters with no phase separation. The presence of a liquid phase, observed in the former scenario, can also be interpreted as the limit of large cluster size ($n \to \infty$), where the adsorption isotherm (Equation (6)) takes the form of a step function indicative of a first-order transition between liquid and gaseous states in the confinement.

3.4. Implications for Liquid Spring Operation

3.4.1. Reversibility

The distinction between the behaviors of the two types of prototypical systems discussed in the preceding paragraph is important as the intrusion/extrusion process along the adsorption isotherm avoids the metastabilities commonly present when liquid extrusion proceeds through liquid evaporation [12,39–43]. In the latter and more common scenario, the undercompressed adsorbate tends to persist in the pores in a metastable liquid state [24,40,44]. When pressure reduction to ambient conditions does not trigger expulsion, the system behaves as a 'bumper', whereas expulsion at extrusion pressure $P_{\text{ex}} < P_{\text{in}}$ results in 'shock absorber' behavior [3–5]. An example of a 'shock absorber' is provided by our model system with methanol intruding 9.5 Å micropores (Figure 5) at bulk pressure $P_{\text{in}} \approx 150$ bar while expulsion takes place at extrusion pressure $P_{\text{ex}} \approx 95$ bar. This means the maximal work that can be recovered represents only a fraction $\eta_{max} \approx P_{\text{ex}}/P_{\text{in}} = 63\%$ of the energy stored in the system upon intrusion. Liquid extrusion from narrower-pore

systems illustrated in Figure 5, on the other hand, represents a reversal of the intrusion through identical states with no hysteresis. The reversibility of the process allows a complete energy recovery ($\eta_{max} \to 1$), although the actual efficiency can still be reduced by friction dissipation at speedy operation. While high interfacial tension of aqueous systems suggests effective storage of surface energy, our model calculations suggest other solvent choices, combined with precise tuning of medium porosity, may prove advantageous by securing reversible cycling operation. In the above examples this is achieved through the use of methanol/lyophilic solid combinations conducive to a gradual adsorption/desorption mechanism of pore filling and emptying free of the vapor nucleation barrier [45,46] associated with extrusion through abrupt evaporation.

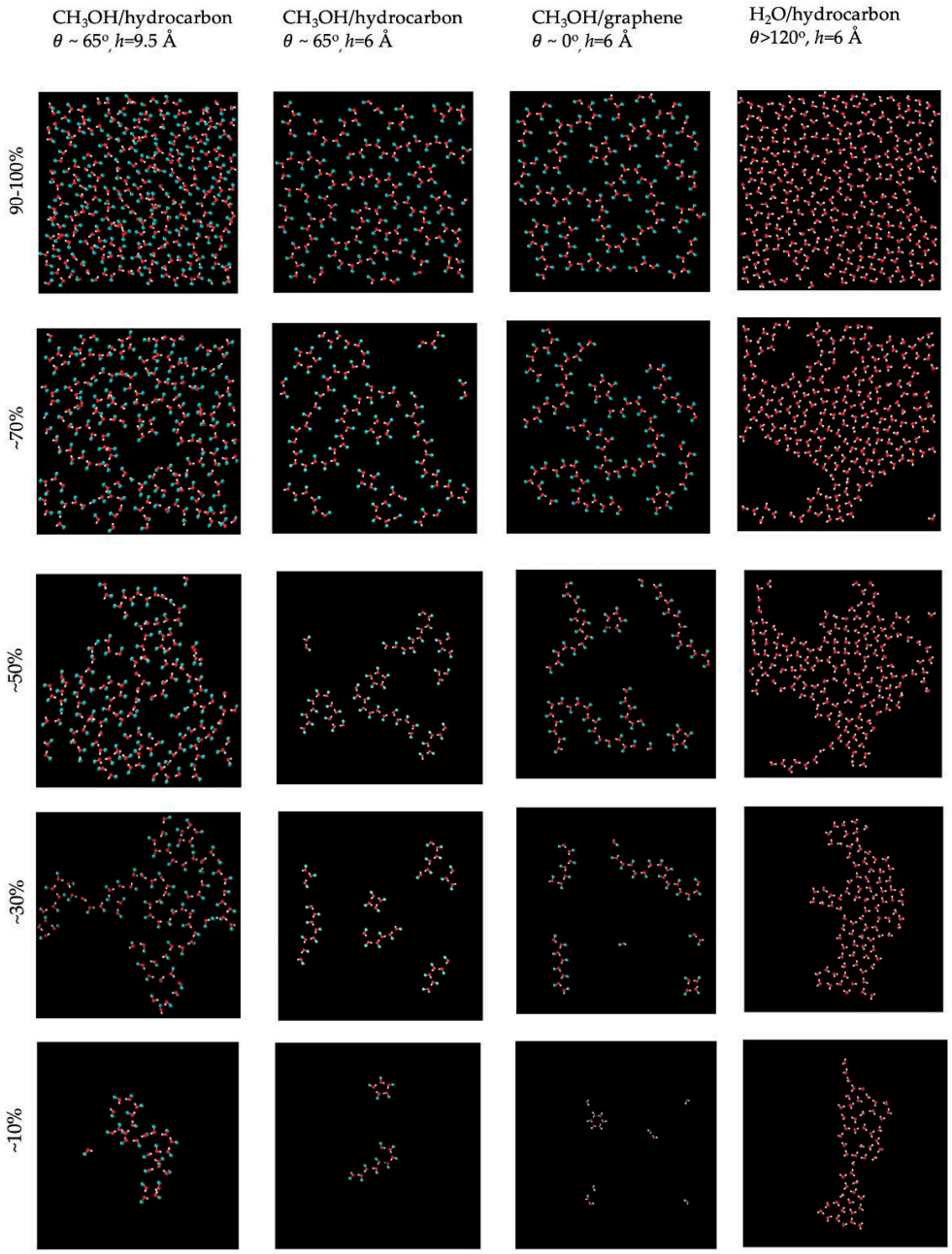

Figure 6. Representative adsorbate (columns 1–3: methanol; column 4: water) configurations in partially filled hydrocarbon or graphene nanopores of diameters 9.5 Å or 6 Å at decreasing loads (top row: near saturation; bottom: approximately 10% filling). Methanol systems are from this work, and aqueous ones (column 4) were obtained by revisiting the situations from an earlier study [12].

3.4.2. Stored Energy Density

Energy E stored in a liquid spring is delivered to the device as pressure/volume work on the piston forcing bulk liquid into adsorbent pores. In this process, the volume of bulk phase, V_b, decreases in proportion to the amount of adsorbed methanol and the work is determined by the expression

$$E = w_{in} = -\int P_b dV_b = -\int P_b \overline{V}(P_b) dN \approx P_{in} \overline{V}(P_{in}) \Delta N = \frac{P_{in} \Delta N}{\rho_b(P_{in})} \quad (7)$$

where dN represents an infinitesimal increment of the number of liquid molecules N adsorbed in the pore and ΔN the maximal change in N in the cycle, $\overline{V}(P_b) = 1/\rho_b(P_b)$ is the pressure-dependent partial molar volume of the liquid in the bulk phase, and intrusion pressure P_{in} the bulk pressure at the inflection point of adsorption isotherms shown in Figure 5. For reversible cycling, the work recovered upon extrusion, w_{ex}, equals $-w_{in}$, whereas hysteresis reduces w_{ex} to $P_{ex}\overline{V}(P_{ex})\Delta N$ where $P_{ex} < P_{in}$ represents the extrusion pressure of the irreversible cycle. Known dependences $N(P_b)$ and $\rho(P_b)$ (Figures 3 and 5 top) enable estimates of stored energy density defined as energy per unit volume of the adsorbent:

$$E_{density} = \frac{E}{V_{ads}} = \frac{E}{L_{xy}^2(h + \delta_w)} \quad (8)$$

where E stands for stored energy (Equation (7)) in the simulation box, and we estimate the corresponding adsorbent volume by the product of the lateral box area L_{xy}^2 times the height $h + \delta_w$ corresponding to the average distance between the midplanes of parallel pores in the adsorbent. Figure 7 presents ballpark estimates for limiting energy densities in the six liquid spring systems illustrated in Figure 5, obtained by Equations (7) and (8) with a reasonable assumption $\delta_w \approx 1$ nm, and values ΔN approximated by $<N>$ at the beginning of the plateau regime of filled pores, $\Delta N \cong 2 < N(P_{in}) >$. Based on these results, energy densities achievable in methanol/carbon-based systems using pressures of up to 2.7 kbar are comparable to those in advanced supercapacitors and can be improved further by manipulation of porosity for higher pressure operation.

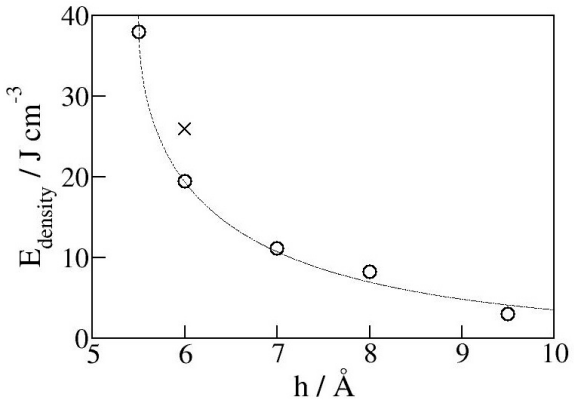

Figure 7. Energy densities in microporous hydrocarbon (O) or graphene (×) adsorbents for a range of pore widths h from 5.5 to 9.5 Å, estimated from GCMC adsorption isotherms $<N(P_b)>$ (Figure 5) and Equation (8) with $\delta_w \approx 1$ nm. The curve serving as a guide to the eye fits hydrocarbon systems.

Using similar diameters h, alternative pore geometry of the adsorbent, e.g., cylindrical, should not modify the qualitative picture or significantly alter the above estimates. A rapid increase in storage capacity is generally expected once the width h is reduced below around $2\sigma_C$, where σ_C denotes the contact distance between the wall and methanol carbon atoms. While the precise values also depend on the force field and require validation in experiment,

the trend appears robust and indicates potential for high storage capacity irrespective of nominal lyophilicity of the materials we consider. The somewhat higher energy density between the more wettable graphene surfaces (Figure 7) can be attributed to the relative hardness of graphene compared to softer hydrocarbons. Liquid/wall interaction potentials $u(z)$ for the two materials indeed confirm the repulsion at small distances z to be stronger for graphene (Figure 2) because of its higher atom surface density, along with steeper $u(\Delta z)$ scaling, approximately proportional [17,47,48] to Δz^{-10} as opposed to $\sim\Delta z^{-9}$ for a flat hydrocarbon surface [22]. While our examples concern neat wall materials, wall/liquid interactions can be tailored in a continuous fashion by using composite materials and functionalization [49,50]. Unless in the linear regime, attraction and lyophilicity will normally exceed the component average if there exist spatial fluctuations around uniform material's composition or coverage [51–53]. While not explicitly addressed in present simulations, robustness at elevated pressures will also play an important role in materials' selection for envisaged experimental work.

4. Concluding Remarks

Through steric restrictions, molecular-scale porosity can render a material effectively lyophobic, and therefore capable of storing surface energy upon wetting irrespective of high wettability measured on flat surfaces. In the present work, this scenario is exemplified by favorable liquid spring performance in methanol/hydrocarbon and methanol/graphene pores studied by open ensemble molecular simulations. In comparison to commonly studied water/hydrophobic pore systems, the above combinations feature stronger wall–liquid adhesion [54] and weaker cohesive forces among liquid molecules. At molecular-size porosity, these differences result in a pressure-controlled adsorption/desorption mechanism best described by Hill's adsorption isotherm, as opposed to an abrupt liquid/vapor phase transition characteristic of water-based liquid springs at any porosity. While the two-phase scenario involves activation barriers resulting in hysteresis with potentially incomplete energy recovery, the adsorption/desorption process we observe manifests complete reversibility, along with absorbed energy densities that are comparable to experimental values [10,11] in aqueous systems. The study establishes the feasibility of liquid spring design using a broadened range of adsorbent materials, whose selection can prioritize mechanical strength to sustain higher compression as the limiting factor for specific energy storage and power capacities of the system.

Author Contributions: Conceptualization, D.B.; methodology, software, and validation, D.B. and A.S.; investigation, D.B. and A.S.; writing—draft preparation, D.B.; writing—review and editing, A.S.; visualization, A.S. and D.B.; project administration, D.B. All authors have read and agreed to the published version of the manuscript.

Funding: A.S. was supported through the Virginia Commonwealth University section of the Federal Work Study program. Computational resources were provided by the National Science Foundation under award CHE-1800120, and computing allocation from the National Energy Research Scientific Computing Center (NERSC) funded by the Office of Science of the U.S. Department of Energy (No. DEAC02-05CH11231).

Data Availability Statement: The data supporting the conclusions is contained within the article or will be made available by the authors upon reasonable request.

Conflicts of Interest: The authors declare no conflicts of interest.

References

1. Eroshenko, V.; Regis, R.C.; Soulard, M.; Patarin, J. Energetics: A new field of applications for hydrophobic zeolites. *J. Am. Chem. Soc.* **2001**, *123*, 8129–8130. [CrossRef]
2. Grosu, Y.; Mierzwa, M.; Eroshenko, V.A.; Pawlus, S.; Chorazewski, M.; Nedelec, J.M.; Grolier, J.P.E. Mechanical, Thermal, and Electrical Energy Storage in a Single Working Body: Electrification and Thermal Effects upon Pressure-Induced Water Intrusion Extrusion in Nanoporous Solids. *ACS Appl. Mater. Interfaces* **2017**, *9*, 7044–7049. [CrossRef]
3. Bushuev, Y.G.; Lowe, A.R.; Ryzhikov, A.; Wasiak, T.; Burt, M.; Chorazewski, M.; Grosu, Y. Energetic and Structural Insights into Water Confined in Hydrophobic Nanopores. *J. Phys. Chem. C* **2026**, *130*, 2057–2071. [CrossRef]
4. Ryzhikov, A.; Dirand, C.; Astafan, A.; Nouali, H.; Daou, T.J.; Bezverkhyy, I.; Chaplais, G.; Bellat, J.P. Calorimetric Heats of Intrusion of LiCl Aqueous Solutions in Hydrophobic MFI-Type Zeosil: Influence of the Concentration. *Langmuir* **2024**, *40*, 8827–8835. [CrossRef] [PubMed]
5. Fraux, G.; Coudert, F.X.; Boutin, A.; Fuchs, A.H. Forced intrusion of water and aqueous solutions in microporous materials: From fundamental thermodynamics to energy storage devices. *Chem. Soc. Rev.* **2017**, *46*, 7421–7437. [CrossRef] [PubMed]
6. Le Donne, A.; Tinti, A.; Amayuelas, E.; Kashyap, H.K.; Camisasca, G.; Remsing, R.C.; Roth, R.; Grosu, Y.; Meloni, S. Intrusion and extrusion of liquids in highly confining media: Bridging fundamental research to applications. *Adv. Phys. X* **2022**, *7*, 2052353. [CrossRef]
7. Rowlinson, J.S.; Widom, B. *Molecular Theory of Capillarity*; Dover: Mineola, NY, USA, 2013.
8. Evans, R. Fluids Adsorbed in Narrow Pores—Phase-Equilibria and Structure. *J. Phys. Condens. Matter* **1990**, *2*, 8989–9007. [CrossRef]
9. Almeida, A.B.; Buldyrev, S.; Alencar, A.M.; Giovambattista, N. How Small Is Too Small for the Capillarity Theory? *J. Phys. Chem. C* **2021**, *125*, 5335–5348. [CrossRef]
10. Grosu, Y.; Li, M.; Peng, Y.L.; Luo, D.; Li, D.; Faik, A.; Nedelec, J.M.; Grolier, J.P. A Highly Stable Nonhysteretic {Cu-2(tebpz) MOF plus water} Molecular Spring. *Chem. Phys. Chem.* **2016**, *17*, 3359–3364. [CrossRef]
11. Confalonieri, G.; Daou, T.J.; Nouali, H.; Arletti, R.; Ryzhikov, A. Energetic Performance of Pure Silica Zeolites under High-Pressure Intrusion of LiCl Aqueous Solutions: An Overview. *Molecules* **2020**, *25*, 2145. [CrossRef]
12. Bratko, D. Reversible Surface Energy Storage in Molecular-Scale Porous Materials. *Molecules* **2024**, *29*, 664. [CrossRef]
13. Frenkel, D.; Smit, B. *Understanding Molecular Simulation: From Algorithms to Applications*, 2nd ed.; Academic Press: San Diego, CA, USA, 2023.
14. Allen, M.P.; Tildesley, D.J. *Computer Simulation of Liquids*; Oxford University Press: New York, NY, USA, 2017.
15. Shelley, J.C.; Patey, G.N. Boundary condition effects in simulations of water confined between planar walls. *Mol. Phys.* **1996**, *88*, 385–398. [CrossRef]
16. Geim, A.K.; Novoselov, K.S. The rise of graphene. *Nat. Mater.* **2007**, *6*, 183–191. [CrossRef]
17. Striolo, A.; Chialvo, A.A.; Cummings, P.T.; Gubbins, K.E. Water adsorption in carbon-slit nanopores. *Langmuir* **2003**, *19*, 8583–8591. [CrossRef]
18. Chen, B.; Potoff, J.J.; Siepmann, J.I. Monte Carlo calculations for alcohols and their mixtures with alkanes. Transferable potentials for phase equilibria. 5. United-atom description of primary, secondary, and tertiary alcohols. *J. Phys. Chem. B* **2001**, *105*, 3093–3104. [CrossRef]
19. Bratko, D.; Daub, C.D.; Leung, K.; Luzar, A. Effect of field direction on electrowetting in a nanopore. *J. Am. Chem. Soc.* **2007**, *129*, 2504–2510. [CrossRef]
20. Ojaghlou, N.; Bratko, D.; Salanne, M.; Shafiei, M.; Luzar, A. Solvent-Solvent Correlations across Graphene: The Effect of Image Charges. *Acs Nano* **2020**, *14*, 7987–7998. [CrossRef]
21. Thornton, M.E.; Zamfir, S.G.; Bratko, D. Wettability of Two-Dimensional Carbon Allotropes from Molecular Simulations. *Molecules* **2025**, *30*, 3296. [CrossRef]
22. Lee, C.Y.; McCammon, J.A.; Rossky, P.J. The Structure of Liquid Water at an Extended Hydrophobic Surface. *J. Chem. Phys.* **1984**, *80*, 4448–4455. [CrossRef]
23. Lee, S.H.; Rossky, P.J. A Comparison of the Structure and Dynamics of Liquid Water at Hydrophobic and Hydrophilic Surfaces—A Molecular-Dynamics Simulation Study. *J. Chem. Phys.* **1994**, *100*, 3334–3345. [CrossRef]
24. Bratko, D.; Curtis, R.A.; Blanch, H.W.; Prausnitz, J.M. Interaction between hydrophobic surfaces with metastable intervening liquid. *J. Chem. Phys.* **2001**, *115*, 3873–3877. [CrossRef]
25. Yeh, I.C.; Berkowitz, M.L. Ewald summation for systems with slab geometry. *J. Chem. Phys.* **1999**, *111*, 3155–3162. [CrossRef]
26. Deleeuw, S.W.; Perram, J.W.; Smith, E.R. Simulation of Electrostatic Systems in Periodic Boundary-Conditions. 1. Lattice Sums and Dielectric-Constants. *Proc. Roy. Soc.* **1980**, *373*, 27–56.
27. Zamfir, S.G.; Moucka, F.; Bratko, D. High-Pressure Infiltration−Expulsion of Aqueous NaCl in Planar Hydrophobic Nanopores. *J. Phys. Chem. C* **2020**, *124*, 23433–23445. [CrossRef]
28. Adams, D.J. Chemical potential of hard-sphere fluid by Monte Carlo methods. *Mol. Phys.* **1974**, *28*, 1241–1252. [CrossRef]

29. Adams, D.J. Grand Canonical Monte Carlo for Lennard Jones fluid. *Mol. Phys.* **1975**, *29*, 307–311. [CrossRef]
30. Bratko, D.; Blanch, H.W. Competition between protein folding and aggregation: A three-dimensional lattice-model simulation. *J. Chem. Phys.* **2001**, *114*, 561–569. [CrossRef]
31. Taylor, J.R. *An Introduction to Error Analysis*; University Science Books: Mill Valley, CA, USA, 1997.
32. Gloor, G.J.; Jackson, G.; Blas, F.J.; de Miguel, E. Test-area simulation method for the direct determination of the interfacial tension of systems with continuous or discontinuous potentials. *J. Chem. Phys.* **2005**, *123*, 134703. [CrossRef] [PubMed]
33. Machado, J.R.S.; Streett, W.B. Equation of State and Thermodynamic Properties of Liquid Methanol from 298 to 489 K and Pressures to 1040-Bar. *J. Chem. Eng. Data* **1983**, *28*, 218–223. [CrossRef]
34. Gromnitskaya, E.L.; Stal'gorova, O.V.; Yagafarov, O.F.; Brazhkin, V.V.; Lyapin, A.G.; Popova, S.V. Ultrasonic study of the phase diagram of methanol. *JETP Lett.* **2004**, *80*, 597–601. [CrossRef]
35. Giovambattista, N.; Almeida, A.B.; Alencar, A.M.; Buldyrev, S.V. Validation of Capillarity Theory at the Nanometer Scale by Atomistic Computer Simulations of Water Droplets and Bridges in Contact with Hydrophobic and Hydrophilic Surfaces. *J. Phys. Chem. C* **2016**, *120*, 1597–1608. [CrossRef]
36. Tinti, A.; Giacomello, A.; Meloni, S.; Casciola, C.M. Classical nucleation of vapor between hydrophobic plates. *J. Chem. Phys.* **2023**, *158*, 134708. [CrossRef]
37. Dill, K.A.; Bromberg, S. *Molecular Driving Forces*, 2nd ed.; Garland Science: New York, NY, USA, 2010.
38. Gesztelyi, R.; Zsuga, J.; Kemeny-Beke, A.; Varga, B.; Juhasz, B.; Tosaki, A. The Hill equation and the origin of quantitative pharmacology. *Arch. Hist. Exact Sci.* **2012**, *66*, 427–438. [CrossRef]
39. Lum, K.; Chandler, D. Phase diagram and free energies of vapor films and tubes for a confined fluid. *Int. J. Thermophys.* **1998**, *19*, 845–855. [CrossRef]
40. Lum, K.; Chandler, D.; Weeks, J.D. Hydrophobicity at small and large length scales. *J. Phys. Chem. B* **1999**, *103*, 4570–4577. [CrossRef]
41. Leung, K.; Luzar, A. Dynamics of capillary evaporation. II. Free energy barriers. *J. Chem. Phys.* **2000**, *113*, 5845–5852. [CrossRef]
42. Leung, K.; Luzar, A.; Bratko, D. Dynamics of capillary drying in water. *Phys. Rev. Lett.* **2003**, *90*, 065502. [CrossRef]
43. Sharma, S.; Debenedetti, P.G. Evaporation rate of water in hydrophobic confinement. *Proc. Natl. Acad. Sci. USA* **2012**, *109*, 4365–4370. [CrossRef] [PubMed]
44. Giovambattista, N.; Rossky, P.J.; Debenedetti, P.G. Effect of pressure on the phase behavior and structure of water confined between nanoscale hydrophobic and hydrophilic plates. *Phys. Rev. E* **2006**, *73*, 041604. [CrossRef] [PubMed]
45. Luzar, A. Activation barrier scaling for the spontaneous evaporation of confined water. *J. Phys. Chem. B* **2004**, *108*, 19859–19866. [CrossRef]
46. Tinti, A.; Giacomello, A.; Casciola, C.M. Vapor nucleation paths in lyophobic nanopores. *Eur. Phys. J. E* **2018**, *41*, 52. [CrossRef] [PubMed]
47. Jaffe, R.L.; Gonnet, P.; Werder, T.; Walther, J.H.; Koumoutsakos, P. Water-carbon interactions—2: Calibration of potentials using contact angle data for different interaction models. *Mol. Simul.* **2004**, *30*, 205–216. [CrossRef]
48. Steele, W.A. *The Interaction of Gases with Solid Surfaces*; Pergamon Press: Oxford, UK, 1974.
49. Wang, J.; Bratko, D.; Luzar, A. Probing surface tension additivity on chemically heterogeneous surfaces by a molecular approach. *Proc. Natl. Acad. Sci. USA* **2011**, *108*, 6374–6379. [CrossRef] [PubMed]
50. Tang, Q.; Zhou, Z.; Chen, Z.F. Graphene-related nanomaterials: Tuning properties by functionalization. *Nanoscale* **2013**, *5*, 4541–4583. [CrossRef]
51. Bratko, D.; Chakraborty, A.K.; Shakhnovich, E.I. Frozen phases of random heteropolymers in disordered media. *Phys. Rev. Lett.* **1996**, *76*, 1844–1847. [CrossRef]
52. Acharya, H.; Ranganathan, S.; Jamadagni, S.N.; Garde, S. Mapping Hydrophobicity at the Nanoscale: Applications to Heterogeneous Surfaces and Proteins. *Faraday Discuss.* **2010**, *146*, 353. [CrossRef]
53. Wu, J.Z.; Bratko, D.; Blanch, H.W.; Prausnitz, J.M. Interaction between oppositely charged micelles or globular proteins. *Phys. Rev. E* **2000**, *62*, 5273–5280. [CrossRef]
54. Israelachvili, J.N. *Intermolecular and Surface Forces*, 3rd ed.; Academic Press: London, UK, 2011.